Disorder-induced suppression of charge density wave order: STM study of Pd-intercalated ErTe₃

Alan Fang [1,2,3] Joshua A. W. Straquadine,[2,3] Ian R. Fisher,[1,2,3] Steven A. Kivelson,[1,2,4] and Aharon Kapitulnik[1,2,3,4]

[1]*Stanford Institute for Materials and Energy Sciences, SLAC National Accelerator Laboratory,*
2575 Sand Hill Road, Menlo Park, California 94025, USA
[2]*Geballe Laboratory for Advanced Materials, Stanford University, Stanford, California 94305, USA*
[3]*Department of Applied Physics, Stanford University, Stanford, California 94305, USA*
[4]*Department of Physics, Stanford University, Stanford, California 94305, USA*

Pd-intercalated ErTe₃ is studied as a model system to explore the effect of increasing disorder on an incommensurate two-component charge density wave (CDW). The ordering vectors of the CDW components lie along the two in-plane principal axes of the nearly tetragonal crystal structure. Using scanning tunneling microscopy (STM), we show that introducing Pd intercalants (i.e., disorder) induces CDW dislocations, which appear to be associated with each CDW component separately. Increasing Pd concentration has a stronger effect on the secondary CDW order, manifested in a higher density of dislocations, and thus increases the anisotropy (nematic character) of the CDW. Suggestive evidence of Bragg glass phases at weak disorder is also discussed.

I. INTRODUCTION

Charge-ordered states are a key feature of strongly correlated materials [1–3]. For example, the cuprate high-temperature superconductors exhibit various signatures of charge ordering and fluctuating order, raising the question of their impact on the occurrence and nature of superconductivity. While notionally "charge order" refers to states that spontaneously break the spatial symmetries of the host crystal, the presence of unavoidable disorder complicates the situation. On theoretical grounds [4] it is expected that even weak quenched disorder disrupts long-range incommensurate charge density wave (CDW) order at long distances, which implies intrinsic difficulty in inferring from observations what the exact form of the symmetry breaking would be in the "ideal," zero-disorder limit [5,6]. This, and the fact that the magnitude of the resulting ion displacements is relatively small, delayed the identification of such order in the cuprates with traditional methods, such as x-ray scattering, even though evidence of local order was deduced earlier from scanning tunneling microscopy (STM) and spectroscopy (STS) studies [7,8].

More generally, because charge order is so sensitive to quenched randomness, it is extremely important to complement spatially averaged information obtained from transport or diffraction measurements with information from local probes. Thus, to shed light on this issue, we turn here to a model system which mimics certain aspects of the main features of the charge-ordering phenomena of the cuprates but for which a fairly solid understanding of the theory of the pure system exists (see [9] and the Supplementary Information of [10]) and disorder can be introduced in a controlled fashion and its effects studied using both global (scattering and transport) and local (STM) probes.

It was recently suggested that Pd-intercalated RTe₃ ($R =$ rare-earth element, Er in this paper) is a suitable model system

[11–13]. This family of quasi-two-dimensional (quasi-2D) metals exhibits unidirectional and bidirectional incommensurate charge density wave states [14–17]. As indicated in Fig. 1, the pristine (unintercalated) compound undergoes two successive CDW phase transitions, with critical temperatures $T_{\mathrm{CDW1}} = 270$ K and $T_{\mathrm{CDW2}} = 165$ K [17]. T_{CDW1} marks the onset of the "primary" CDW order with ordering vector q_{CDW1}, and T_{CDW2} is the second, orthogonal CDW component with q_{CDW2}. Thus, despite the nearly tetragonal symmetry of the crystal, the phase at $T_{\mathrm{CDW1}} > T > T_{\mathrm{CDW2}}$ has unidirectional CDW order, while the low-temperature phase is bidirectional, but with generally inequivalent strengths. Straquadine and Fisher demonstrated via resistivity measurements that signatures of the two phase transitions are then smeared and suppressed by Pd intercalation, consistent with a scenario in which the dominant effect arises from disorder induced by the intercalant atoms [13].

In this paper we present a low-temperature STM study of the effects of disorder on the two orthogonal components of the incommensurate CDW order in Pd-intercalated ErTe₃. This allows us to obtain clear insight into the nature of the interplay between the two components of the order, the relation between the fundamental density wave order and composite orientational ("vestigial nematic" [9]) order, and the (sometimes nonlocal) role of topological defects (dislocations) in all these phenomena. Our principal results are as follows: (i) Both CDWs resolved by STM are consistent with bulk measurements [13,18], including the fact that the wavelengths in the two directions are slightly but significantly different from each other. (ii) Both CDW components coexist throughout the sample, even in the presence of disorder, consistent with the intrinsically bidirectional character of the low-temperature CDW order. However, the CDW associated with the higher T_c is dominant. (iii) Introducing Pd intercalants induces both phase disorder and dislocations (initially dislocation pairs), which appear to be associated with each component
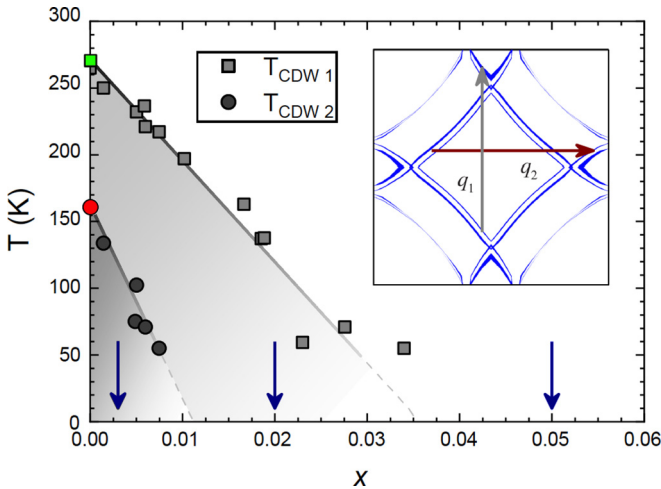
235446-1

FIG. 1. Phase diagram taken from [13]. Colored points at $x = 0$ mark the phase transitions of the pristine sample. Gray points at finite x mark the crossover temperatures identified as features in the electrical resistivity. Vertical arrows mark the three Pd concentrations discussed in this paper. Inset: Calculated Fermi surface of the parent compound ErTe$_3$ (from [15]) with q_1 and q_2 as nesting vectors.

separately. This has a stronger disruptive effect on the secondary CDW, which has a greater number of dislocations than the primary component. (iv) Nonetheless, vestiges of the two distinct CDW phases persist all the way to 5% Pd intercalation, far beyond where signatures of the smeared phase transitions are observed in bulk probes. (v) In the presence of disorder, nematic order [9,10] is still preserved over length scales at least as long as the STM field of view. We propose a phase diagram with two Bragg glass [19–24] phases and speculate where our samples fall on this diagram.

RTe$_3$ is formed in the orthorhombic space group C_{mcm} [25] and contains double layers of nominally square Te planes separated by RTe block layers. Orthorhombicity is derived from a glide plane stacking of these tetragonal layers, which determine the electronic properties of this system at high temperatures. A unidirectional CDW was first detected in this system by transmission electron microscopy [14]. Angle-resolved photoemission spectroscopy (ARPES) showed that large portions of the Fermi surface (FS) nested by $\mathbf{q}_{CDW1}$ are indeed gapped [26]. STM and STS studies established the incommensurate nature of the CDW in TbTe$_3$ while also revealing an additional CDW ordering perpendicular to the principal one [16], but weaker in amplitude. Subsequent ARPES studies on ErTe$_3$ established that two incommensurate CDW gaps are created in two separate transitions by perpendicular FS nesting vectors [18]. Despite the near-nesting conditions that result in gapping of a substantial portion of the Fermi surface in the CDW state, several factors indicate that strong-coupling effects unrelated to Fermi surface nesting play a role [27]. Evidence for this perspective lies in the large values of $2\Delta_{CDW}/k_B T_{CDW}$ ($\sim$15 and $\sim$7 for the first and second CDWs, respectively) [28], although several other factors can also yield such an effect. More convincingly, high-energy-resolution inelastic x-ray scattering on TbTe$_3$ revealed strong phonon softening and increased phonon linewidths over a large part in reciprocal space adjacent to the CDW ordering

vector, thus showing momentum-dependent electron-phonon coupling [29].

II. EXPERIMENT

Pd$_x$ErTe$_3$, with $0 \leqslant x \leqslant 0.055$, was grown using a Te self-flux for pure RTe$_3$ compounds [15], with the addition of small amounts of Pd to the melt. A detailed description of sample preparation, characterization, and the effect of Pd intercalation on the bulk properties is given in [13]. Three levels of intercalation were studied: 0.3%, 2%, and 5% (marked in Fig. 1). STM was performed with a hybrid UNISOKU-USM1300 system constructed with a homemade ultrahigh-vacuum sample preparation and manipulation system. The samples were cleaved at room temperature at pressures of low 10^{-10} torr and immediately transferred to the low-temperature STM. Topography was performed at $\approx$ 1.7 K, with typical tunneling parameters of $V_{bias} = 50$–100 mV and $I = 100$–300 pA.

III. RESULTS AND DISCUSSION

The phase diagram in Fig. 1 shows that the secondary CDW state is more sensitive to disorder. Its "transition temperature" is suppressed quickly as x increases and extrapolates to zero around $x = 1\%$. Thus, samples with low levels of intercalants should be an excellent starting point to observe the effect of weak disorder on both transitions.

Figure 2(a) shows the topography of an $x = 0.3\%$ sample. The features visible are an atomic corrugation, CDW corrugations, and small lumps on the surface, often with a skewed X pattern around them. The lumps, which generally increase in number with the intercalation density, are only a fraction of an angstrom high and thus must arise from subsurface intercalants rather than surface Pd atoms. Single-crystal x-ray diffraction on the same crystals confirmed the increase in the b-axis lattice constant consistent with Pd atoms intercalating between the van der Waals bonded Te bilayer [13]. Density functional theory calculations also show this to be the most favorable location for intercalation [11]. No surface Pd atoms were observed for low intercalations, presumably due to the high volatility of the Pd atoms upon cleaving at room temperature.

Much of the analysis of the CDW and effects of disorder is done via the Fourier transform (FFT) of the topographic data, as in Fig. 2(b). The two CDWs generate a series of very sharp peaks in a line from the origin to both reciprocal lattice points corresponding to the RTe block layer [see Figs. 2(c) and 2(f)]. As in previous STM and x-ray studies of the parent compound [15,16,30], there are four characteristic CDW points due to mixing with the lattice. For the primary (dominant) CDW, these are $q_{CDW1} = 0.70c^*$, $c^* - q_{CDW1} = 0.30c^*$, $2c^* - 2q_{CDW1} = 0.60c^*$, and $2q_{CDW1} - c^* = 0.40c^*$. [In this material, the primary and secondary CDWs lie along the c and a axes, respectively, and the asterisk (*) indicates the reciprocal lattice vector.] The perpendicular line cut has a slightly different set of peaks with $q_{CDW2} = 0.68a^*$, $a^* - q_{CDW2} = 0.32a^*$, etc. (The uncertainty is $\approx 0.005c^*$, or one FFT pixel, in our 100-nm scans.) Based on wavelength, we identify the former with the primary, or higher T_c, CDW
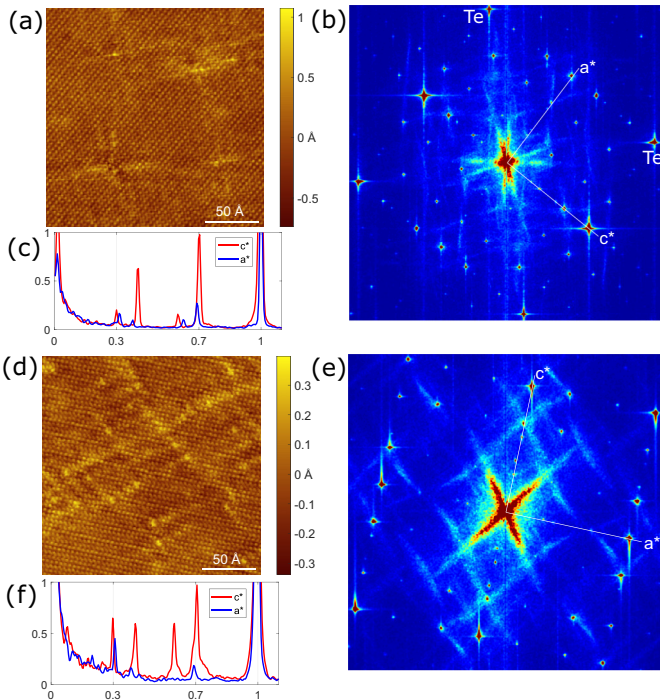
FIG. 2. (a) Topography (cropped) of the 0.3% Pd-intercalation sample. (A full-size 100-nm image is available in Appendix A). (b) FFT of (a) with reciprocal lattice points from the Te plane labeled and white lines indicating the line cut directions. (c) The respective line cuts. Here the stronger CDW peaks (red) are along c^*. (d) Topography (cropped) of the 2% sample. (e) FFT of (d) and (f) the respective line cuts.
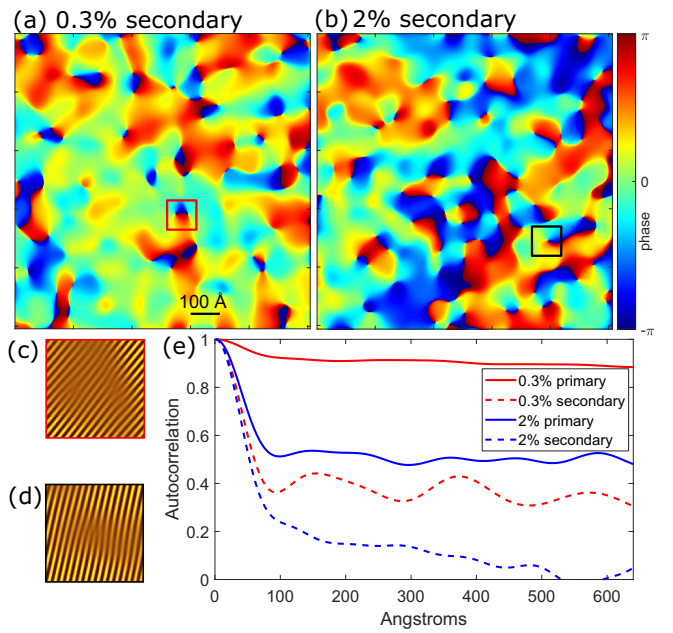

FIG. 3. CDW defect analysis of the 0.3% and 2% Pd-intercalation samples. (a) The 1000-Å phase plot for the 0.3% secondary CDW showing dislocations. (b) The 2% sample. (c) and (d) Zooms of the highlighted areas showing real-space filtered topography. (e) Autocorrelation plots for the CDW signals.

[17,18,31]. The latter is the secondary CDW, with a transition at lower temperatures, and is the one that shows a weaker signal in diffraction measurements and disappears first with rising intercalation level [13]. In our STM data, depending on many factors, such as tunneling parameters, tip condition, and scan location, the relative amplitudes of the four peaks within one line scan can vary. However, it is generally true that the CDW1 signal is always stronger everywhere in the 0.3% sample, thus giving the visual impression of a unidirectional CDW. We also note the presence of strong satellite peaks at $\mathbf{q}_{Te} \pm \mathbf{q}_{CDW}$. The CDW exists in the Te plane, and its signal is strongly modulated by this lattice ($\mathbf{q}_{Te}$). Similar strong satellites were also seen in the STM data of pristine TbTe$_3$ [16].

Next, we show a higher level (2%) of intercalation in Figs. 2(d)–2(f), where the secondary CDW is expected (from resistivity data) to be absent. Like in the 0.3% sample, we note the lack of surface Pd atoms. There also exist the same subangstrom lumps, the X pattern, and their greater abundance in accordance with the higher intercalation level. However, both CDWs are still present, with the second CDW having a lower amplitude. This was also seen in the low-temperature x-ray data of [13]. For either intercalation level, both CDWs are omnipresent, ruling out the possibility of alternating domains of a unidirectional CDW.

Unlike the parent compound, the presence of intercalants creates additional features in the topography and FFT due to quasiparticle scattering interference. In real space, this

manifests itself as streaks that emanate from some of the lumps in a skewed X pattern. In Fourier space, scattering along ungapped portions of the Fermi surface, which generally run ≈45° to the CDW vectors (Fig. 1, inset), manifests as a compressed X at the origin as well as other streaks. This X is biased in the c^* direction in the 2% sample and may reflect the broken fourfold symmetry via two different CDW gaps [18]. In the 0.3% sample there are two of these features, perpendicularly overlapped.

To focus on the distinct CDW components, we decompose the topographic maps in Figs. 2(a) and 2(d) as $\rho(\mathbf{r}) = \rho_1(\mathbf{r}) + \rho_2(\mathbf{r}) + \cdots$, where the primary component, $\rho_1(\mathbf{r})$, is obtained by applying a flat-topped Gaussian filter that keeps only Fourier components in a neighborhood of radius Δq around $q_{CDW1} = 0.70c^*$, $\rho_2(\mathbf{r})$ is obtained from the same filtering near $q_{CDW2} = 0.68a^*$, and $\cdots$ is everything else. (All data shown are for $\Delta q \approx 0.05c^*$ to avoid capturing portions of the nearby CDW point. Further details regarding the filter width and subsequent data analysis are provided in Appendix A.) Each component, in turn, can be expressed in terms of an amplitude and phase, $\rho_j(\mathbf{r}) = A_j(\mathbf{r}) \cos[\mathbf{q}_{CDWj} \cdot \mathbf{r} + \phi_j(\mathbf{r})]$, where the phase measures the lateral displacements in the CDW structure, and dislocations are visualized where the phase winds by 2π around a point. The majority of dislocations are paired with a nearby antidislocation so that the phase winding cancels out. The phase ϕ_2 of the secondary CDW (the one more strongly affected by disorder) in the 0.3% and 2% samples is shown in Figs. 3(a) and 3(b), respectively. Figures 3(c) and 3(d) show $\rho_2(\mathbf{r})$ in the small areas identified by the squares in Figs. 3(a) and 3(b), which contain, respectively, a dislocation pair and an isolated dislocation. The primary CDW in the 0.3% sample has minimal phase
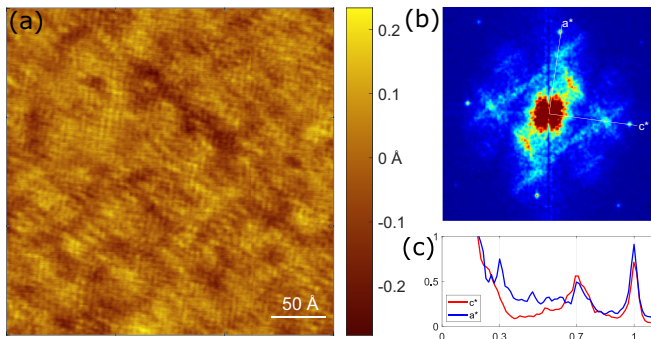
FIG. 4. (a) The 300-Å topography of the 5% Pd-intercalation sample. (b) FFT of (a) and (c) the respective line cuts.

FIG. 5. A proposed phase diagram as derived in Appendix B.

variations and no dislocations, meaning that the intercalants have a minimal effect on this CDW (see Fig. 7). In the 2% sample, the primary CDW has some closely separated dislocation pairs, but no isolated dislocations were observed.

To obtain a more quantitative measure of the range of the CDW correlations we compute the autocorrelation of the filtered CDW

$$G_j(\mathbf{r}) \equiv \mathrm{Re}\left[g_j \int d^2\mathbf{r}' A_j(\mathbf{r}) A_j(\mathbf{r}+\mathbf{r}') e^{i\phi_j(\mathbf{r}) - i\phi_j(\mathbf{r}+\mathbf{r}')} \right], \quad (1)$$

with normalization g_j chosen such that $G_j(\mathbf{0}) = 1$. This quantity is shown in Fig. 3(e) for both the primary (solid lines) and secondary (dashed lines) components of the CDW and for both the 2% (blue) and 0.3% (red) samples. Manifestly, out to the longest distances accessible to us, it is clear that the disorder has a substantially stronger effect on the secondary CDW, but that, with the possible exception of the secondary CDW in the 2% sample, long-range correlations persist even in the presence of disorder. The character of the short distance drop in G_j, unsurprisingly, depends on the choice of Δq and is due to non-CDW features or noise which create short-range correlations. [Oscillations in the curves are due to analyzing individual data sets and thus lack (disorder) configuration averaging.] However, the qualitative doping dependence of the long-distance (greater than 100 Å) correlation is relatively insensitive to these factors, as shown in Fig. 8 in Appendix A.

Finally, we discuss the 5% Pd-intercalation sample, where Fig. 1 would suggest that remnants of both CDWs are completely suppressed. The topography in Fig. 4(a) is qualitatively different from that in the lower intercalation samples, lacking the skewed X pattern, but still having subangstrom height modulations with small length-scale corrugations. We typically observe an adatom on the surface approximately once every 30 nm, with a height of a few angstroms, which occasionally moves or causes a tip reconstruction. This limits our scan size and therefore FFT resolution.

The FFT [Fig. 4(b)] reveals that the CDW peaks are now significantly broadened, with a vague grouping near the primary CDW point and an even more nebulous region for the secondary one. However, broad peaks at the CDW ordering vector still appear in the line cuts in Fig. 4(c). At higher temperatures (95 K), no sharp k-space points were seen in x-ray and electron diffraction measurements[13]. Instead,
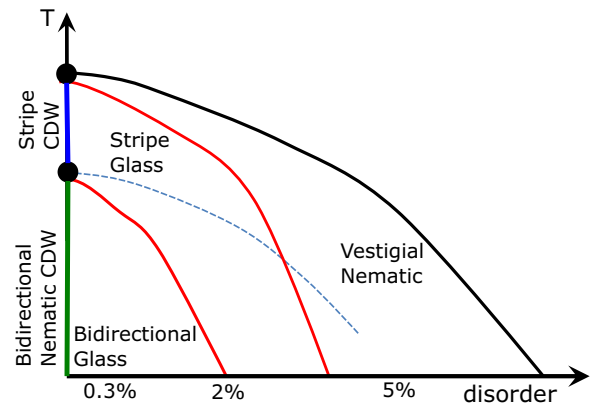
broad and diffuse streaks spanning between the original CDW points were seen, indicating 2D short-range correlations that are consistent with the q-dependent susceptibility. What could be these same streaks appear in our data as well. In fact, the visible corrugations seen in the topography are due to these streaks plus the broad CDW peaks and not the atomic lattice, although the lattice points are well defined in the FFT. This short-range CDW order likely originates from CDW fluctuations pinned by the disorder as the sample is cooled to measurement temperature [3]. A similar observation was reported for the CDW system NbSe$_2$ [32].

Putting all these results together, we propose a phase diagram for a two-component CDW system in the presence of disorder (derivation and further explanation are given in Appendix B) as in Fig. 5. Viewing this in terms of STM data, in the less disordered samples, the decay of the CDW correlations at long distances (up to $r \sim 1000$ Å) is sufficiently slow that it could be consistent with persistent long-range order, but we rule this interpretation out on theoretical grounds. In contrast, in three dimensions, a Bragg glass phase is thought [22] to be possible, in which the autocorrelation function falls as a power law, $\sim 1/r^x$, with $x \approx 1$, and in which no isolated (unpaired) dislocations would occur at long distances. We thus identify as Bragg glass order cases in which no isolated dislocations are seen in the field of view and in which the autocorrelation function at long distances is approximately constant or, at most, very slowly decreasing. In both the 0.3% and 2% samples but not in the 5% sample, the primary (dominant) CDW component exhibits Bragg glass correlations by this criterion. The secondary (subdominant) CDW also is Bragg-glass-like in the 0.3% sample, meaning the ground state is a bidirectional Bragg glass. By contrast, in the 2% sample, we see fairly well isolated dislocations in the secondary CDW, and the correlations fall considerably with distance, meaning that either the CDW is short range correlated and thus the ground state is a unidirectional "stripe glass" or that the sample is at least close to the phase boundary. In the 5% sample, all the CDW correlations are short ranged, but there still is a notable difference between the strength and range of the two components, so (to the extent that the effect of the weak orthorhombicity can be treated as a perturbation) this sample exhibits vestigial nematic order.
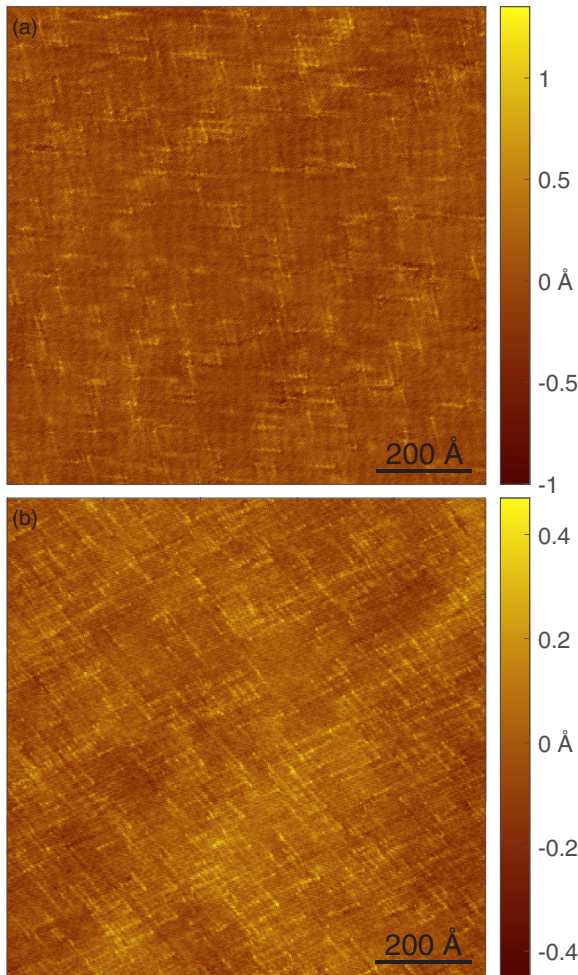
FIG. 6. The 1000-Å topographic images for (a) the 0.3% Pd-intercalation sample and (b) the 2% sample.
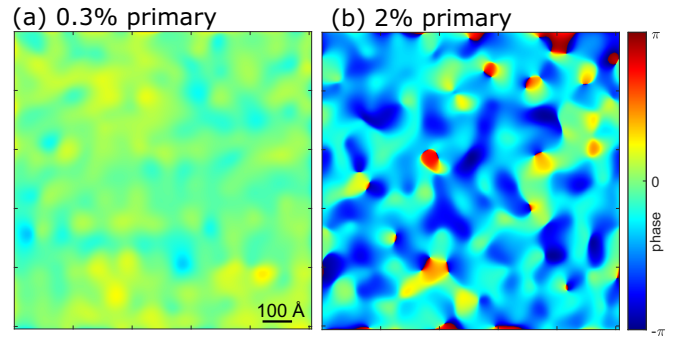

FIG. 7. The 1000-Å phase plots for (a) the 0.3% Pd-intercalation sample and (b) the 2% sample.

real-space representation of the CDW, we reverse transform to obtain $\rho(\mathbf{r})$. To obtain the phase plots, we additionally multiply by $e^{-i\mathbf{q}_{CDW}\cdot\mathbf{r}}$ and take the angle of this complex quantity. Two phase plots (for the primary CDW component) not shown in the main body of the paper are provided in Fig. 7. Note that these have fewer dislocations than their respective secondary components. In particular, the 0.3% primary CDW has a relatively uniform phase and no dislocations at all.

To compute autocorrelation, we use the Fourier-filtered CDW signal $\rho(\mathbf{r})$. This results in a 2D image, peaked at the center, with modulations at the CDW period. In order to remove the oscillations and obtain the amplitude, we multiply by $e^{-i(\mathbf{q}_{CDW}\cdot\mathbf{r}+\delta)}$ and filter away the second harmonic. The resultant image has both real and imaginary components, and via careful choice of $\mathbf{q}_{CDW}$ and δ, the real part can be maximized with minimal imaginary contributions. That this is possible is a testament to the single-frequency (i.e., long correlation length) nature of the CDW. Using the real image, we take a line cut from the origin out in the direction of the CDW with a small angular average ($\pm 7°$) for smoothing.

APPENDIX A: ADDITIONAL DATA AND ANALYSIS OF DISLOCATIONS

Figure 6 shows the full-range topographic data for the 0.3% and 2% samples. We start by employing a variant of the Fujita-Lawler analysis of a localized Fourier transform in order to get local displacements of the atomic lattice which are related to scanning artifacts such as creep and hysteresis [33,34]. The distortion is removed before further analysis.

Next, we Fourier transform the topographic data and filter around the $q_{CDW} = 0.70c^*$ (or $0.68a^*$) point. To obtain a
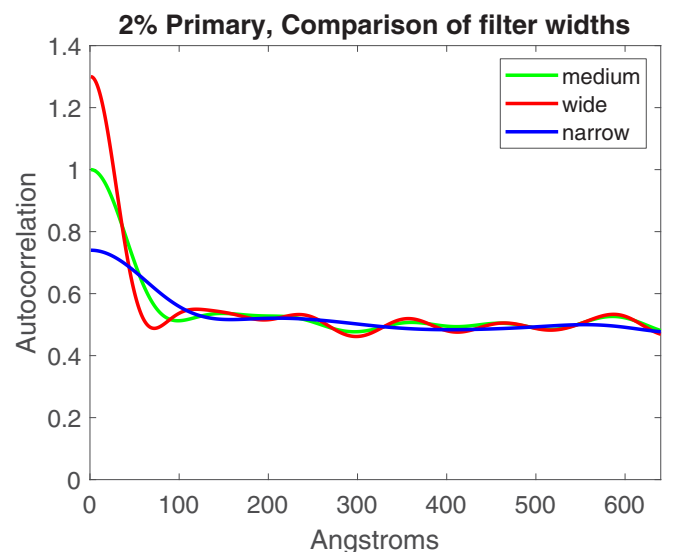

FIG. 8. Effect of varying the Fourier filter width around the CDW point when computing autocorrelation. "Medium" filter width is used in the main body of the paper.

In Fig. 8 we show the effects of the Fourier filter width Δq around the CDW point on the calculation of autocorrelation. The green "medium" curve corresponds to the filter width used in the main body of the paper and all the analyses. In this plot, the autocorrelation curves have been normalized at long length scales. A wider filter lets in more high-frequency noise and other spurious signals, which leads to more short-length correlations (the initial peak in the red curve) as well as unphysical oscillations.

APPENDIX B: THEORETICAL BACKGROUND

In this Appendix we provide a summary of the theoretical background behind our analyses of the experimental data. It sketches an effective field theory of two-component CDW order in the presence of quenched randomness. In reality, the crystals involved are slightly orthorhombic, but this seems to be a very small effect, so we will consider an idealization in which the crystal is taken to be tetragonal and the orthorhombicity—when included at all—will be represented as an infinitesimal external symmetry-breaking field.

1. Reviewing the phase diagram in the clean limit

In the absence of disorder (or the best achievable approximation to this limit) the phase diagram in T and chemical pressure P shows three distinct phases: a uniform (no CDW) phase for $T > T_{\text{CDW1}}(P)$; a phase with "bidirectional" CDW order, but with distinctly different strengths and slightly different ordering vectors for the two CDW components at $T < T_{\text{CDW2}}(P) < T_{\text{CDW1}}(P)$; and a "unidirectional" CDW for intermediate temperatures $T_{\text{CDW1}}(P) > T > T_{\text{CDW2}}(P)$. Both CDW phases break the tetragonal point-group symmetry and in this sense have a nematic component.

Since the two transitions are separated from each other, it is reasonable to treat them separately. However, since the various ordering tendencies get both truncated and scrambled when disorder is introduced, we would like to treat them from the perspective of a single, unified effective field theory. Moreover, it is observed that as a function of increasing P, the two lines tend to approach one another, so that for the case of ErTe$_3$ studied here (which has the largest effective P, i.e., the smallest lattice constant of any of the stoichiometric tri-tellurides studied to date) $(T_{\text{CDW1}} - T_{\text{CDW2}})/T_{\text{CDW1}} \approx 0.4$. We would thus like to think that this allows us to organize our thinking about a putative multicritical point at $T = T^* > 0$ and $P = P^*$ at which these two lines would meet at slightly higher pressure, i.e., $T_{\text{CDW1}}(P^*) = T_{\text{CDW2}}(P^*) = T^*$.

The nature of such a multicritical point in a tetragonal system is already somewhat unusual. To see this, consider the lowest-order effective (Landau) potential as a function of the two components of the CDW order represented by two complex scalar fields, ϕ_1 and ϕ_2. To the extent that the crystal can be treated as approximately tetragonal, the effective Hamiltonian density $\mathcal{H}[\phi_1, \phi_2]$ is symmetric under discrete rotations (and other point group interactions) that exchange ϕ_1 and ϕ_2. (The weak effect of the subtle orthorhombicity of the actual crystal structure can be modeled as a small symmetry-breaking term of the form $\mathcal{V}_{orth} \equiv -b[|\phi_1|^2 - |\phi_2|^2]$.)
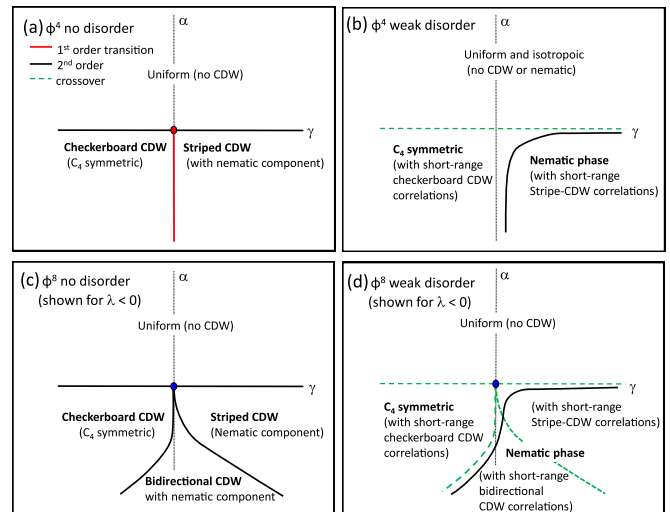

FIG. 9. Steps in constructing the phase diagram which is the result of the minimization of the different parts of the effective potential (see text).

2. ϕ^4 theory of stripe and nematic phases

To fourth order in the fields, the effective potential is

$$\mathcal{V}(\phi_1, \phi_2) = \frac{\alpha}{2}[|\phi_1|^2 + |\phi_2|^2] + \frac{1}{4}[|\phi_1|^2 + |\phi_2|^2]^2$$
$$+ \frac{\gamma}{2}|\phi_1|^2|\phi_2|^2 + \cdots, \qquad (B1)$$

where we have assumed that the quartic term is positive and have normalized the fields such that their strength is unity.

The phase diagram in the α-γ plane that results from minimizing this effective potential (i.e., Landau theory) is shown in Fig. 9(a). For $\gamma > 0$, there is a second-order transition to a stripe-ordered CDW phase as α changes from positive to negative values, while for $\gamma < 0$ the transition is to a checkerboard state. In the stripe phase, either the thermal average of ϕ_1 is nonzero and $\phi_2 = 0$ or the converse; in addition to breaking translational symmetry in one direction, this phase strongly breaks the C_4 rotational symmetry that interchanges the two components of the order parameter. In the checkerboard phase, the thermal averages of ϕ_1 and ϕ_2 are not only nonzero but of equal magnitude; this state breaks translation symmetry in both directions but leaves an unbroken C_4 rotational symmetry. The point $\alpha = \gamma = 0$ is a bicritical point, below which, as a function of γ, there is a first-order boundary between the stripe and checkerboard phases. Fluctuation effects for an effective Landau-Ginzburg-Wilson model with this form of the effective potential have been considered elsewhere (see especially [9]). In addition to their effects on critical exponents, these can lead to additional subtleties in the nature of the phase diagram and even to additional phases making their appearances; for instance, in a quasi-2D system, there can be a narrow strip between the stripe-ordered phase and the fully symmetric phase in which CDW order is melted but in which vestigial C_4 symmetry breaking persists, giving rise to a vestigial nematic phase.

More interesting is what happens to this phase diagram in the presence of weak but non-negligible disorder. Here (in $d \leqslant 4$) no incommensurate CDW long-range order is possible, which likely implies that the CDW transitions are all replaced by crossover lines separating regions with little in the way of CDW correlations from regions with substantial intermediate-range CDW order. (An interesting possibility, which we will ignore for now but to which we will return below, is that for weak enough disorder there could exist a Bragg glass phase with power-law CDW order and no unbound dislocations [22,23].) However, as shown in Ref. [9] (and as would be expected anyway on general grounds), the nematic component of the stripe order persists up to a nonvanishing critical disorder strength. The shape of the phase boundary follows from continuity: in the limit that the disorder strength tends to zero, this boundary must coincide with the phase boundary of whatever CDW phase has a nematic component. Thus, the phase diagram in the presence of weak disorder becomes that in Fig. 9(b), where the dashed lines indicate crossovers, and the solid black line bounds the nematic phase.

3. ϕ^8 theory and the nematic bidirectional CDW phase

Manifestly, the ϕ^4 theory is inadequate in that it is missing one phase that is observed in experiments (the nematic bidirectional CDW) and yet has one implied phase (the checkerboard CDW) not seen in experiments. While we can always imagine that the checkerboard CDW is lurking, as yet undiscovered, in the large-P reaches of the phase diagram, the missing bidirectional phase is something that needs to be addressed.

Even in the case of pure ErTe$_3$, T_{CDW2} is smaller than T_{CDW1} by a substantial factor, so at temperatures in the neighborhood of T_{CDW2} there is no justification for assuming that $|\phi_j|$ is small; there is thus no reason to keep only low-order terms in powers of the field in the effective field theory. Indeed, away from the putative multicritical point, it is legitimate to treat the two clean-limit transitions in terms of two distinct effective field theories. Let us consider the case where we are well below T_{CDW1}, where the value of either $|\phi_1|$ or $|\phi_2|$ is not small, but above T_{CDW2}, and even slightly below T_{CDW2}, the subdominant component is a legitimate expansion parameter. It is convenient to carry out the expansion of the effective potential in a way that is still manifestly C_4 invariant. We thus define new quantities as follows: $\phi_1 \equiv |\phi| \cos(\theta) e^{i\delta_1}$ and $\phi_2 \equiv |\phi| \sin(\theta) e^{i\delta_2}$. Translational symmetry implies that the free energy must be independent of δ_1 and δ_2, and the tetragonal symmetry implies that the free energy must be invariant under $\theta \to -\theta$ and $\theta \to \theta + \pi/2$. We can therefore, in complete generality, express the effective potential in terms of the two quantities $|\phi|^2 \equiv |\phi_1|^2 + |\phi_2|^2$ and $\Delta^4 \equiv |\phi_1|^2|\phi_2|^2 = |\phi|^4[1 - \cos(4\theta)]/8$, such that near T_{CDW2}, Δ is small. We thus expand $\mathcal{V}$ in powers of Δ, giving

$$\mathcal{V} = \mathcal{V}_0(|\phi|^2) + \frac{\mathcal{V}_1(|\phi|^2)}{2}\,\Delta^4 + \frac{\mathcal{V}_2(|\phi|^2)}{4}\Delta^8 + \cdots, \quad \text{(B2)}$$

where (noting explicitly for future use all terms up to order $|\phi|^8$ and using the same conventions for the low-order terms as above)

$$\mathcal{V}_0(\phi^2) = \frac{\alpha}{2}\phi^2 + \frac{1}{4}\phi^4 + \frac{u_6}{6}\phi^6 + \frac{u_8}{8}\phi^8 + \cdots, \quad \text{(B3)}$$

$$\mathcal{V}_1(\phi^2) = \gamma + \frac{\gamma_2}{2}\phi^2 + \frac{\gamma_4}{4}\phi^4 \cdots, \quad \text{(B4)}$$

$$\mathcal{V}_2(\phi^2) = \lambda + \cdots. \quad \text{(B5)}$$

In the neighborhood of T_{CDW2}, $|\phi|$ is already large and does not change much in magnitude, so we can focus exclusively on θ. For $V_1 > |V_2||\phi|^4/4$, $\mathcal{V}$ is minimal for $\theta = 0$ (i.e., we are in the stripe phase), while for $V_1 < -|V_2||\phi|^4/4$ the minimum is at $\theta = \pi/4$ (i.e., we are in the checkerboard phase). (Here $[\theta]$ means the value of θ mod $\pi/2$ chosen to lie in the interval $0 \leqslant [\theta] < \pi/2$.) The shape of this intermediate regime depends on the sign of V_2. For $V_2 < 0$ [the case illustrated in Fig. 9(c)], in the interval $0 < V_1 < |V_2||\phi|^4$,

$$\theta = \frac{1}{4}\cos^{-1}\left[\frac{|V_2||\phi|^4 - 8V_1}{|V_2||\phi|^4}\right]. \quad \text{(B6)}$$

Thus, the boundary between the stripe phase and the nematic bidirectional CDW phase (i.e., the line that implicitly defines T_{CDW2}) occurs where $V_1 = 4|V_2|\phi|^4$, while the boundary between the nematic bidirectional CDW phase and the checkerboard phase occurs where $V_1 = 0$. On the other hand, for $V_2 > 0$, the stripe phase persists as long as $V_1 > 0$. Thus, T_{CDW2} is defined by the condition $V_1 = 0$, while the transition to the checkerboard phase occurs where $V_1 = -V_2|\phi|^4/4$. In both cases, all transitions are continuous.

For simplicity, this discussion was carried through in the case in which T_{CDW2} is well separated from T_{CDW1}. However, clearly, the same considerations apply even as they approach each other at the multicritical point, $\alpha = \gamma = 0$. All that is different here is that the size of the intermediate nematic bidirectional CDW phase, which is bounded by $|\delta\mathcal{V}_1| < |\mathcal{V}_2|\phi|^4/4$, thus gets to be parametrically small, as shown in Fig. 9(c). Here, approximating these terms by their leading-order expressions in powers of $|\phi|^2$, we infer that the intermediate phase occurs for a range of γ such that $|\gamma| \lesssim |\lambda||\alpha|^2$.

It is interesting to note that the instability of the bicritical point seen in the ϕ^4 treatment and its substitution by this peculiar tetracritical point appears to be inevitable, at least at the level of mean-field theory. We have not explicitly carried out the analogous treatment of fluctuation effects and the effects of disorder in the resulting ϕ^8 theory as was carried out for the ϕ^4 theory. Away from the multicritical point, however, more or less the same considerations apply, leading to the (conjectural) phase diagram shown in Fig. 9(d) in the presence of weak disorder.

Indeed, at the conjectural level, it is reasonable to propose that as a function of T and disorder strength σ, one would expect a phase diagram with the general topology shown in Fig. 10. Here, the inset shows a portion of the clean limit phase diagram (plotted in the α-γ plane, where α should be considered a proxy for T), and the dotted red line shows a trajectory through this diagram at fixed γ such that the two requisite transitions at T_{CDW1} and T_{CDW2} are present. The main figure assumes the same fixed γ but shows a putative
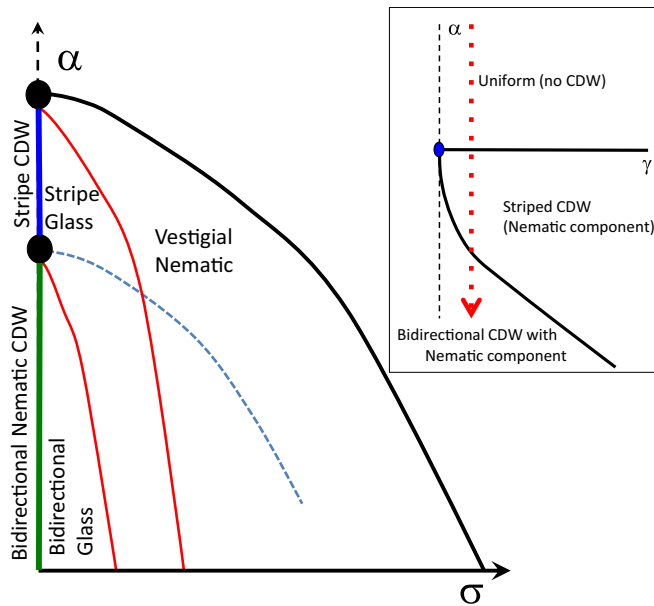
FIG. 10. A conjectured phase diagram as a function of temperature T and disorder strength σ. Here the inset shows a portion of the clean-limit phase diagram (plotted in the α-γ plane, where α should be considered a proxy for T; see text).

phase diagram in the α-σ plane. Phases with CDW long-range order are confined to the $\sigma = 0$ axis. However, in just the same way as previously discussed [9], the disorder leaves us with a nematic transition, represented by the solid black line, that survives up to a critical value of σ, defined as the point at which the nematic critical temperature goes to zero. Strong local CDW correlations persist to finite disorder, vanishing with increasing α or σ via a crossover that can be roughly identified with the nematic transition line, although surely some local correlations survive arbitrarily far beyond this. No other symmetries are broken upon decreasing α, so what was T_{CDW2} at $\sigma = 0$ becomes a crossover line (which is sharply defined only for arbitrarily weak disorder), below which a second component of the local CDW correlations should be apparent. (This is indicated by the dashed blue line in Fig. 10.)

Finally, we have indicated two possible Bragg-glass transitions in Fig. 10 as solid red lines. A Bragg glass is characterized by quasi-long-range (power law) order and an absence of any free dislocations [22,23]. It is thermodynamically distinct from a CDW phase (which has long-range order) and from a fully disordered phase (which has exponentially falling CDW correlations). The existence or not of such a phase is not inevitable, as it depends on an appropriate hierarchy of energies (e.g., a large core energy for the dislocation) but it is thought to be possible in three dimensions. In the present case there could be two such phases: one being a "stripe-glass phase" (discussed previously in Ref. [35]) in which there is unidirectional CDW quasi-long-range order and a "bidirectional glass phase" which has two orthogonal, nonequivalent CDW correlations, both with quasi-long-range order. In principle, such quasi-long-range order could be inferred from x-ray diffraction as it leads to a charge-order peak which has a power-law singularity, which is distinct from the δ function that rises from long-range-order or the Lorentzian (or squared Lorentzian) that characterizes the disordered phase. While this distinction is likely difficult to establish in practice, a more promising way to establish such a phase is from STM studies in which dislocations can be directly visualized.

In terms of other (non-STM) measurement techniques, the red lines mark thermodynamic phase transitions, so nonanalytic behavior of any measurable properties should appear as one crosses them. What those singularities are is not simple to predict unambiguously. Moreover, because these are glassy states, the issue of dynamics is always present to complicate any discussion—these systems are prone to fall out of equilibrium due to all sorts of domain pinning phenomena—which would also round any thermodynamic signatures. The phase boundaries (solid lines) in Fig. 10 should show up as sharp features in measurable quantities, under conditions in which the system remains in equilibrium. The nematic transition, however, should be rounded by the small degree of orthorhombicity in the crystals: it should thus show best as a relatively sharp onset of various measures of macroscopic anisotropy, such as anisotropy in the resistivity tensor. The red lines are intrinsically glassy and so may be associated with the onset of slow glassy dynamics and a failure of the system to achieve equilibrium on laboratory timescales.

[1] E. Fradkin, S. A. Kivelson, and J. M. Tranquada, *Colloquium*: Theory of intertwined orders in high temperature superconductors, [Rev. Mod. Phys. **87**, 457 (2015)](#).

[2] B. Keimer, S. A. Kivelson, M. R. Norman, S. Uchida, and J. Zaanen, From quantum matter to high-temperature superconductivity in copper oxides, [Nature (London) **518**, 179 (2015)](#).

[3] S. A. Kivelson, I. P. Bindloss, E. Fradkin, V. Oganesyan, J. M. Tranquada, A. Kapitulnik, and C. Howald, How to detect fluctuating stripes in the high-temperature superconductors, [Rev. Mod. Phys. **75**, 1201 (2003)](#).

[4] Y. Imry and S.-K. Ma, Random-Field Instability of the Ordered State of Continuous Symmetry, [Phys. Rev. Lett. **35**, 1399 (1975)](#).

[5] J. A. Robertson, S. A. Kivelson, E. Fradkin, A. C. Fang, and A. Kapitulnik, Distinguishing patterns of charge order: Stripes or checkerboards, [Phys. Rev. B **74**, 134507 (2006)](#).

[6] A. Del Maestro, B. Rosenow, and S. Sachdev, From stripe to checkerboard ordering of charge-density waves on the square lattice in the presence of quenched disorder, [Phys. Rev. B **74**, 024520 (2006)](#).

[7] C. Howald, H. Eisaki, N. Kaneko, M. Greven, and A. Kapitulnik, Periodic density-of-states modulations in superconducting $Bi_2Sr_2CaCu_2O_{8+\delta}$, [Phys. Rev. B **67**, 014533 (2003)](#).

[8] K. McElroy, D.-H. Lee, J. E. Hoffman, K. M. Lang, J. Lee, E. W. Hudson, H. Eisaki, S. Uchida, and J. C. Davis, Coincidence of Checkerboard Charge order and Antinodal State Decoherence in Strongly Underdoped Superconducting $Bi_2Sr_2CaCu_2O_{8+\delta}$, [Phys. Rev. Lett. **94**, 197005 (2005)](#).

[9] L. Nie, G. Tarjus, and S. A. Kivelson, Quenched disorder and vestigial nematicity in the pseudogap regime of the cuprates, [Proc. Natl. Acad. Sci. USA **111**, 7980 (2014)](#).

[10] H. Jang, W. S. Lee, H. Nojiri, S. Matsuzawa, H. Yasumura, L. Nie, A. V. Maharaj, S. Gerber, Y. J. Liu, A. Mehta, D. A. Bonn, R. Liang, W. N. Hardy, C. A. Burns, Z. Islam, S. Song, J. Hastings, T. P. Devereaux, Z. X. Shen, S. A. Kivelson, C. C. Kao, D. Zhu, and J. S. Lee, Ideal charge-density-wave order in the high-field state of superconducting YBCO, Proc. Natl. Acad. Sci. USA **113**, 14645 (2016).

[11] J. He, P. Wang, H. Yang, Y. Long, L. Zhao, C. Ma, M. Yang, D. Wang, X. Shangguan, M. Xue, P. Zhang, Z. Ren, J. Li, W. Liu, and G. Chen, Superconductivity in Pd-intercalated charge-density-wave rare earth poly-tellurides $RETe_n$, Supercond. Sci. Technol. **29**, 065018 (2016).

[12] R. Lou, Y. Cai, Z. Liu, T. Qian, L. Zhao, Y. Li, K. Liu, Z. Han, D. Zhang, J. He, G. Chen, H. Ding, and S. Wang, Interplay between multiple charge-density waves and the relationship with superconductivity in Pd_xHoTe_3, Phys. Rev. B **93**, 115133 (2016).

[13] J. A. W. Straquadine, F. Weber, S. Rosenkranz, A. H. Said, and I. R. Fisher, Suppression of charge density wave order by disorder in Pd-intercalated $ErTe_3$, Phys. Rev. B **99**, 235138 (2019).

[14] E. DiMasi, M. C. Aronson, J. F. Mansfield, B. Foran, and S. Lee, Chemical pressure and charge-density waves in rare-earth tritellurides, Phys. Rev. B **52**, 14516 (1995).

[15] N. Ru and I. R. Fisher, Thermodynamic and transport properties of YTe_3, $LaTe_3$, and $CeTe_3$, Phys. Rev. B **73**, 033101 (2006).

[16] A. Fang, N. Ru, I. R. Fisher, and A. Kapitulnik, STM Studies of $TbTe_3$: Evidence for a Fully Incommensurate Charge Density Wave, Phys. Rev. Lett. **99**, 046401 (2007).

[17] N. Ru, C. L. Condron, G. Y. Margulis, K. Y. Shin, J. Laverock, S. B. Dugdale, M. F. Toney, and I. R. Fisher, Effect of chemical pressure on the charge density wave transition in rare-earth tritellurides RTe_3, Phys. Rev. B **77**, 035114 (2008).

[18] R. G. Moore, V. Brouet, R. He, D. H. Lu, N. Ru, J.-H. Chu, I. R. Fisher, and Z.-X. Shen, Fermi surface evolution across multiple charge density wave transitions in $ErTe_3$, Phys. Rev. B **81**, 073102 (2010).

[19] M. V. Feigel'man, V. B. Geshkenbein, A. I. Larkin, and V. M. Vinokur, Theory of Collective Flux Creep, Phys. Rev. Lett. **63**, 2303 (1989).

[20] T. Nattermann, Scaling Approach to Pinning: Charge Density Waves and Giant Flux Creep in Superconductors, Phys. Rev. Lett. **64**, 2454 (1990).

[21] J.-P. Bouchaud, M. Mézard, and J. S. Yedidia, Variational Theory for Disordered Vortex Lattices, Phys. Rev. Lett. **67**, 3840 (1991).

[22] T. Giamarchi and P. Le Doussal, Elastic theory of flux lattices in the presence of weak disorder, Phys. Rev. B **52**, 1242 (1995).

[23] M. J. P. Gingras and D. A. Huse, Topological defects in the random-field XY model and the pinned vortex lattice to vortex glass transition in type-II superconductors, Phys. Rev. B **53**, 15193 (1996).

[24] J.-i. Okamoto, C. J. Arguello, E. P. Rosenthal, A. N. Pasupathy, and A. J. Millis, Experimental Evidence for a Bragg Glass Density Wave Phase in a Transition-Metal Dichalcogenide, Phys. Rev. Lett. **114**, 026802 (2015).

[25] B. K. Norling and H. Steinfink, The crystal structure of neodymium tritelluride, Inorg. Chem. **5**, 1488 (1966).

[26] V. Brouet, W. L. Yang, X. J. Zhou, Z. Hussain, N. Ru, K. Y. Shin, I. R. Fisher, and Z. X. Shen, Fermi Surface Reconstruction in the CDW State of $CeTe_3$ Observed by Photoemission, Phys. Rev. Lett. **93**, 126405 (2004).

[27] M. D. Johannes and I. I. Mazin, Fermi surface nesting and the origin of charge density waves in metals, Phys. Rev. B **77**, 165135 (2008).

[28] C. M. Varma and A. L. Simons, Strong-Coupling Theory of Charge-Density-Wave Transitions, Phys. Rev. Lett. **51**, 138 (1983).

[29] M. Maschek, S. Rosenkranz, R. Heid, A. H. Said, P. Giraldo-Gallo, I. R. Fisher, and F. Weber, Wave-vector-dependent electron-phonon coupling and the charge-density-wave transition in $TbTe_3$, Phys. Rev. B **91**, 235146 (2015).

[30] H. Yao, J. A. Robertson, E.-A. Kim, and S. A. Kivelson, Theory of stripes in quasi-two-dimensional rare-earth tellurides, Phys. Rev. B **74**, 245126 (2006).

[31] V. Brouet, W. L. Yang, X. J. Zhou, Z. Hussain, R. G. Moore, R. He, D. H. Lu, Z. X. Shen, J. Laverock, S. B. Dugdale, N. Ru, and I. R. Fisher, Angle-resolved photoemission study of the evolution of band structure and charge density wave properties in RTe_3 (R = Y, La, Ce, Sm, Gd, Tb, and Dy), Phys. Rev. B **77**, 235104 (2008).

[32] C. J. Arguello, S. P. Chockalingam, E. P. Rosenthal, L. Zhao, C. Gutiérrez, J. H. Kang, W. C. Chung, R. M. Fernandes, S. Jia, A. J. Millis, R. J. Cava, and A. N. Pasupathy, Visualizing the charge density wave transition in $2H$-$NbSe_2$ in real space, Phys. Rev. B **89**, 235115 (2014).

[33] M. J. Lawler, K. Fujita, J. Lee, A. R. Schmidt, Y. Kohsaka, C. K. Kim, H. Eisaki, S. Uchida, J. C. Davis, J. P. Sethna, and E.-A. Kim, Intra-unit-cell electronic nematicity of the high-T_c copper-oxide pseudogap states, Nature (London) **466**, 347 (2010).

[34] A. Fang, C. Adamo, S. Jia, R. J. Cava, S.-C. Wu, C. Felser, and A. Kapitulnik, Bursting at the seams: Rippled monolayer bismuth on $NbSe_2$, Sci. Adv. **4**, eaaq0330 (2018).

[35] S. Kivelson and V. Emery, Stripe liquid, crystal, and glass phases of doped antiferromagnets, in *Stripes and Related Phenomena*, edited by A. Bianconi and N. L. Saini, Selected Topics in Superconductivity (Kluwer Academic, Plenum Publishers, New York, 2000), pp. 91–100.